

Ultraviolet Imaging Detectors for the GOLD Mission

O.H.W. Siegmund, J. McPhate, T. Curtis, S. Jelinsky, J.V. Vallerger, J. Hull and J. Tedesco

Space Science Laboratory
University of California, Berkeley, CA 94720-7450

ABSTRACT

The GOLD mission is a NASA Explorer class ultraviolet Earth observing spectroscopy instrument that will be flown on a telecommunications satellite in geostationary orbit in 2018. Microchannel plate detectors operating in the 132 nm to 162 nm FUV bandpass with 2D imaging cross delay line readouts and electronics have been built for each of the two spectrometer channels for GOLD. The detectors are “open face” with CsI photocathodes, providing ~30% efficiency at 130.4 nm and ~15% efficiency at 160.8 nm. These detectors with their position encoding electronics provide ~600 x 500 FWHM resolution elements and are photon counting, with event handling rates of > 200 KHz. The operational details of the detectors and their performance are discussed.

Keywords: microchannel plate, ultraviolet, photon counting, detector.

Correspondence: Email: ossy@ssl.berkeley.edu; Telephone: 510 642-0895

1. INTRODUCTION

The GOLD mission¹ directly addresses an investigation of the dramatic variability in many of the state variables describing the ionosphere-thermosphere-mesosphere region. Operating in geostationary orbit, GOLD will, for the first time, make global-scale images of two critical state variables – thermospheric temperature and composition – on half-hour time scales. Such measurements of the global-scale behavior of the ionosphere-thermosphere allow unambiguous separation of spatial and temporal variability. These data will enable GOLD to determine how the ionosphere-thermosphere system changes in response to geomagnetic storms, solar radiation, and upward propagating tides, enabling closure in understanding the global-scale response of the ionosphere-thermosphere system to external and internal influences. GOLD uses two identical imaging spectrographs to measure the Earth’s airglow emissions from 132 to 162 nm. On the disk, temperature and composition will be obtained from N₂ Lyman-Birge-Hopfield (LBH) band and atomic oxygen 135.6 nm emissions during the day, and electron density will be inferred from the 135.6 nm emissions at night. On the limb, exospheric temperatures will be derived from LBH emission profiles and O₂ density profiles will be derived using stellar occultations. The detectors implemented for GOLD are open face microchannel plate detectors with CsI alkali halide UV photocathodes and two dimensional cross delay line photon counting image readouts with their associated encoding electronics.

2. DETECTOR CONFIGURATION AND DESIGN

The GOLD FUV microchannel plate detectors are open face sensors with a 40mm circular format and use a delay line readout to encode individual photon positions. A model overview of the GOLD detectors is shown in Fig. 1 and a photograph of the flight FM01 detector is shown in Fig. 2. At the input of the detector is a 95% transmissive grid which is biased negatively (using a resistor) with respect to the MCP input, and is implemented to recover emitted photoelectrons from the MCP web area thus increasing the overall quantum efficiency (QE). A Cesium Iodide (CsI) opaque photocathode layer is deposited on the input (top) MCP and is visible to the eye as an interference color pattern (Fig. 2) caused by a gradation in the cathode thickness due to the angle of deposition of the photocathode layer. The MCPs (Fig. 3) are a stack of three 46mm Photonis (Brive) MCPs with 12.5 μm pores, 60:1 l/d and a 19° pore bias angle to optimize quantum efficiency. The MCPs are stacked back to back except that a thin (25 μm thick) aperture mask is placed between the second and the bottom MCPs of the stack to define the field of view of the detector to 27 mm (dispersion direction) x 32 mm (cross dispersion). The internal components are supported mechanically by a brazed ceramic and Kovar body assembly (Fig. 2), and the MCPs are held in place with a spring ring arrangement. The cross

delay line (XDL) readout anode is ~ 6 mm behind the MCP stack, and the MCP to anode gap bias is ~ 600 V to allow several periods of the delay line pattern to be overlapped by each photon event. The delay line anode encodes event positions in both axes. Serpentine conductors are deposited onto a ceramic substrate with isolation layers that allow each orthogonal delay line to intercept about 50% of the incoming charge cloud. The fast signals (~ 5 ns wide) from the MCP propagate to the ends of the anode axes and the difference in arrival times allow determination of the centroid of the original photon location. Similar XDL anodes were used for several prior missions^{2,3}. The delay line anode is clamped into the vacuum flange that supports the detector assembly (Figs. 1, 2) and all four output signals are connected to SMA type signal connectors welded into the vacuum flange. The flange also contains the Reynolds Century input high voltage connector (Fig. 1, right) and Reynolds 600S high voltage return (Fig. 1, left) MCP output connector. The entire detector is installed onto a vacuum housing with a motorized door assembly and window that was supplied by LASP at the University of Colorado. The detector is $\sim 10 \times 9 \times 4$ cm and the mass is ~ 425 g, excluding the housing.

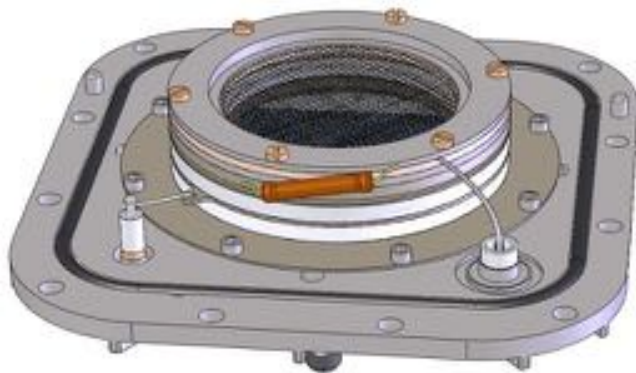


Figure 1: Overview of the GOLD detector showing the input QE enhancement grid, grid bias resistor & high voltage feedthroughs. There are two UV detectors, one for each of the spectrographs.

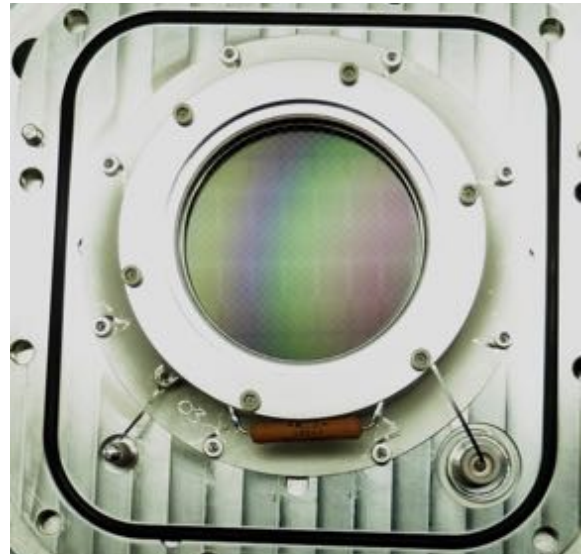


Figure 2: GOLD FM01 detector, showing the CsI photocathode layer (interference colors) input QE enhancement grid, grid bias resistor & high voltage feedthroughs.

High voltage power supplies are provided by LASP at the University of Colorado, and Space Sciences Laboratory (SSL), U.C. Berkeley. SSL designed and built the engineering model position encoding electronics, then the flight model electronics boards were built by LASP at the University of Colorado, and integrated, tested and optimized at SSL. The connections to the electronics from the detectors are short (~ 15 cm) coaxial cables, and all the position encoding electronics is contained within a single stacked module (Fig. 4). The incoming signals are initially amplified by fast (a few ns) amplifiers. The difference in the time of arrival for signals at opposing ends of the delay lines is determined by constant fraction discrimination and time to amplitude conversion, followed by digitization (Fig. 4). An FPGA accomplishes multiple ADC sample averaging per event and packages the resulting event positions for X and Y to be transmitted to the downstream data system. There is also a charge amplifier tap on the input signals, the peak charge signal is digitized and represents the overall charge signal for each amplified photon event. The detector electronics mass is ~ 800 gm, the box size is $\sim 12.5 \times 7.5 \times 9$ cm and consumes ~ 7.3 W.

Characterization for each detector includes measurements of the gain-voltage relationship, single event pulse amplitude distributions, flat field imaging performance and gain map, background count rate and imaging, quantum efficiency (as a function of angle and wavelength, and spatial uniformity) and spatial resolution, image linearity and stability. Environmental tests including shake, thermal and thermal vacuum cycling were also done. A summary of test results for the flight and engineering unit detectors is presented here.

3. PERFORMANCE CHARACTERISTICS

3.1 Gain and Pulse Height Distribution

The single photon counting mode of operation of the GOLD detector system provides a pulse amplitude for each detected photon in addition to each photon's position. The sum of the charge detected on the X and Y axes of the delay line anode is the total charge of the amplified photon event. For the majority of tests performed a UV lamp (185 nm, Hg) was used to stimulate the detector. Typical results for the overall gain as a function of applied voltage to the MCP stack is shown in Figure 5. A gain value is determined using the modal peak of the pulse amplitude distribution (Fig. 6) for an integration of events distributed over the entire face of the detector. The gain characteristics measured for the gain curves (Fig. 5) obtained are in accord with the expected values for a stack of three 60:1 l/d, 12 μm pore MCPs⁴. The variation in applied voltage to achieve the same gain was typically ± 50 V for the majority of the MCPs tested. The nominal operating gain for the GOLD MCP detectors is about 1.6 pC, or 1.05×10^7 , which is achieved at about 950 V per MCP. The pulse height distributions shapes are Gaussian-like (Fig. 6), and provide a well defined amplitude distribution at 10^7 gain that is clearly separated from the lower level threshold of the processing electronics ($< \sim 2 \times 10^6$).

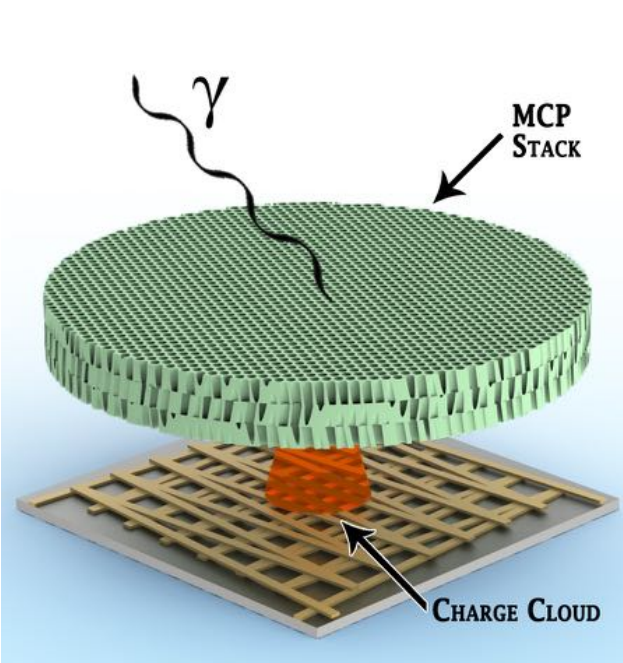


Figure 3: The GOLD detectors function through detection of UV photons by a CsI photo-cathode deposited onto the front of a stack of 3 MCPs. Photons converted to electrons are then multiplied by the MCPs and the resulting charge cloud is sensed and positions are encoded by a cross delay line readout anode.

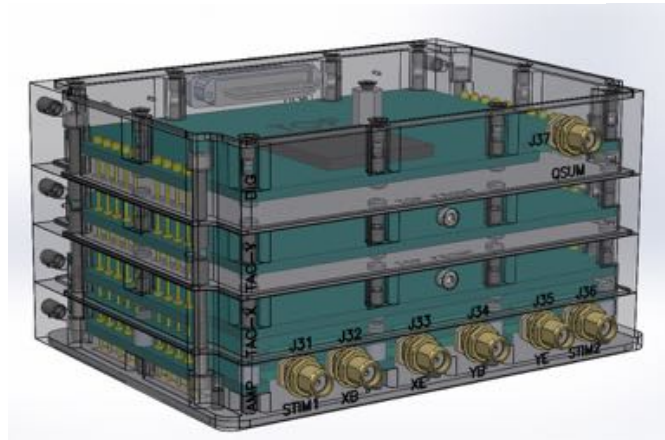
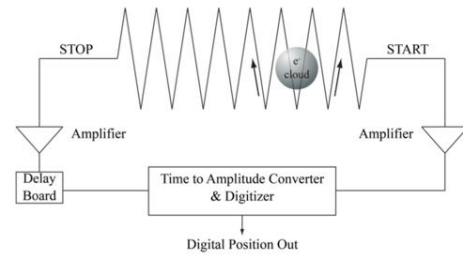


Figure 4: GOLD detector electronics encodes photon X & Y positions by determining the difference in arrival times of the signals at the two ends of each delay line of the cross delay line anode. The package includes front end amplifiers, time to digital converters and an FPGA for data processing and interfacing.

3.2 Background Events

Background event data was collected for all the GOLD detectors. The background pulse amplitude distributions generally show a negative exponential shape (Fig. 7) as compared with the peaked UV photon event pulse amplitude distributions. The intrinsic level⁵ of the background event rate is determined by ⁴⁰K beta decay events due to the potassium content in the MCP glass. These events are generated and detected throughout the bulk of the glass, thus producing an exponentially decreasing pulse amplitude distribution. Dust or debris on the detector can sometimes produce "hot spots" and residual gas ion events if they are present. In such cases peaks in the background distribution can occur at the same amplitude as the UV photons (hot spots on the MCPs) or at slightly higher gains (residual gas ion detection). Both have been seen on GOLD MCP stacks but can be resolved by careful cleaning and ensuring that

operations are at good vacuum pressures ($< 2 \times 10^{-6}$ Torr). Imaging background events can reveal hot spots or field emission problems, but generally the distribution of events is spatially uniform (Fig. 8). The overall rate for GOLD MCP stacks varies somewhat but on average is ~ 0.25 events $\text{cm}^{-2} \text{sec}^{-1}$ which is in accord with expectations for standard MCP material from Photonis (Brive). The expected “in-orbit” background rate is dominated by in-situ radiation detected by the MCPs (both gamma and particle background) and is expected to be of the order of ~ 100 events $\text{cm}^{-2} \text{sec}^{-1}$ in geostationary orbit.

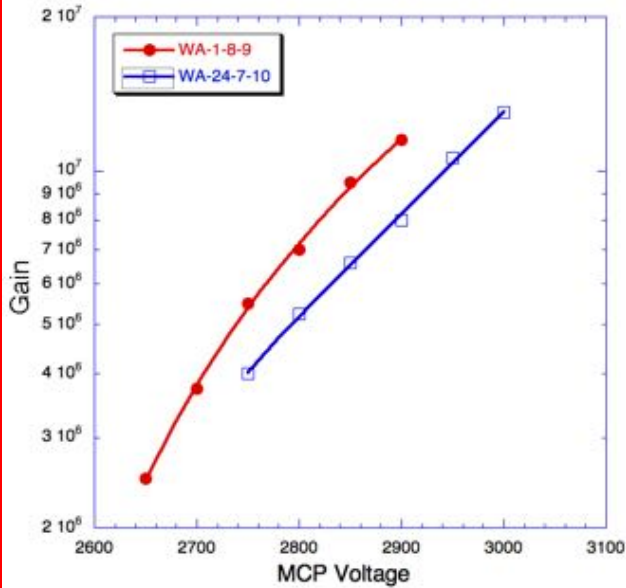


Figure 5: GOLD MCP stack gain as a function of applied voltage for two different stacks. MCPs are a 3 stack of 46mm diameter, with 12 μm pores and 60:1 l/d, and 19° bias angle.

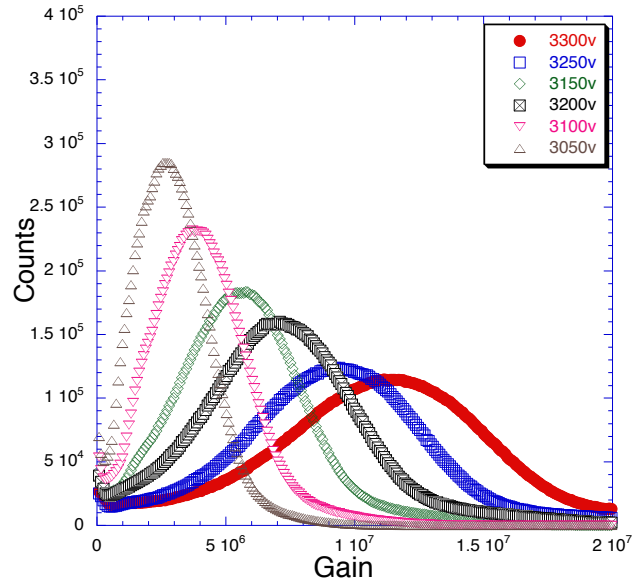


Figure 6: GOLD MCP pulse height distributions for a typical stack show peaked shape with $\sim 70\%$ FWHM at gain of $\sim 10^7$. Bias potential includes 600 V for the MCP to anode gap. 185 nm UV.

3.3 Imaging Characteristics

The GOLD electronics is configured to accommodate photon event centroid position encoding to 4k x 4k bins, however this is scaled to allow event position encoding for stimulation pulses that are well outside the actual image field of view. Consequently, the actual electronic event position binning is approximately 20 μm / bin for the final image map. This results in an effective area of $\sim 1600 \times 1350$ electronic bins for the image. Since the intrinsic point spread resolution function of the electronics and detector is a Gaussian of $\sim 50 \mu\text{m}$ FWHM this allows for binning of the point spread function in accord with Nyquist sampling, producing $\sim 600 \times 500$ FWHM resolution elements. To characterize the flat field a diffuse 185nm UV source was used to evenly illuminate the input MCP at ~ 100 kHz rates using $\sim 1 \times 10^7$ gain. Typical features seen in the flat field are the hexagonal packing patterns of the MCPs^{2,3} and edge distortions due to the electric field fringing from the support ring of the MCPs in the MCP to anode gap. The MCPs used for the GOLD detectors benefit from improvements in MCP fabrication processes and have considerably less hexagonal (Fig. 9) image modulation that is caused by crushing of pores at the edges of the hexagonal packing boundaries. The image modulation is of the order $\sim 7\%$ which is comparable to prior findings⁶ for the current MCP fabrication process. The hexagonal modulation is slightly more apparent in the gain-map image (Fig. 10), where the color of the area is representative of the average gain at that position. The gain at the hexagonal multifiber boundaries is $\sim 10\%$ to 15% lower than the rest of the MCP area. Overall variations of the gain as a function of position are $\sim \pm 20\%$ for most of the GOLD MCP stacks. The use of a mask between the second and third MCP of the MCP stack defines the active area and does not produce field fringing issues at the MCP output surface. Consequently we see very little image distortion at the edges of the field of view except at the upper and lower right corners. This is where the mask comes close to the MCP support flange and the gap field fringing pushes events back towards the image center, causing an edge brightening (Fig. 9) for a small edge area. This is not of any significant concern for the science data acquisition.

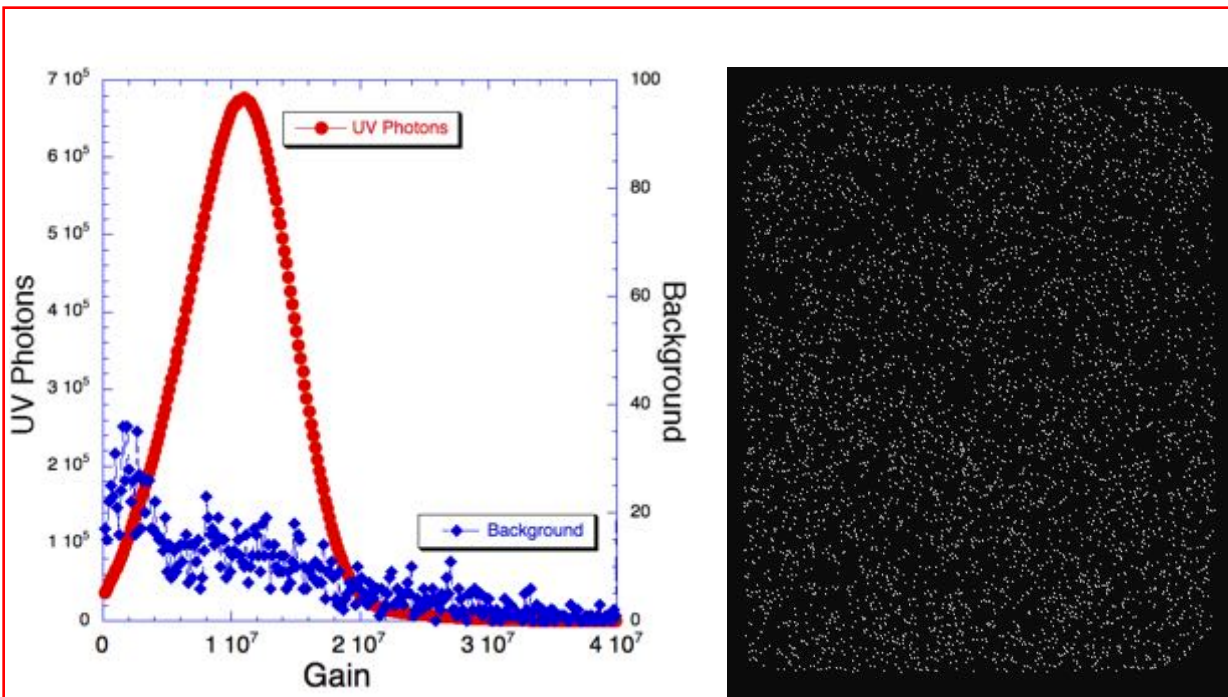


Figure 7: Pulse height distributions for UV photons and background events for a typical GOLD MCP stack. Background events decrease in frequency with increasing amplitude and are predominantly a result of ^{40}K beta decay in the MCP bulk glass.

Figure 8: GOLD FM02 detector (CsI cathode) background event image (1000 s) shows a uniform distribution of events. Average background rates for the GOLD MCP stacks is $\sim 0.25 \text{ events cm}^{-2} \text{ sec}^{-1}$, which is in accord with expectations for these MCPs.

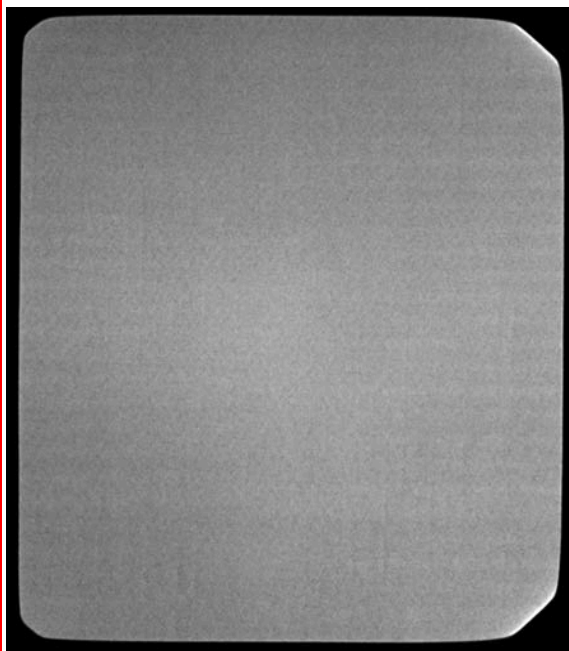


Figure 9: Full field 185 nm UV illumination of the GOLD FM03 detector, showing the low level of image modulation due to the MCP multi-fibers (measured at $\leq 7\%$) (6×10^7 events).

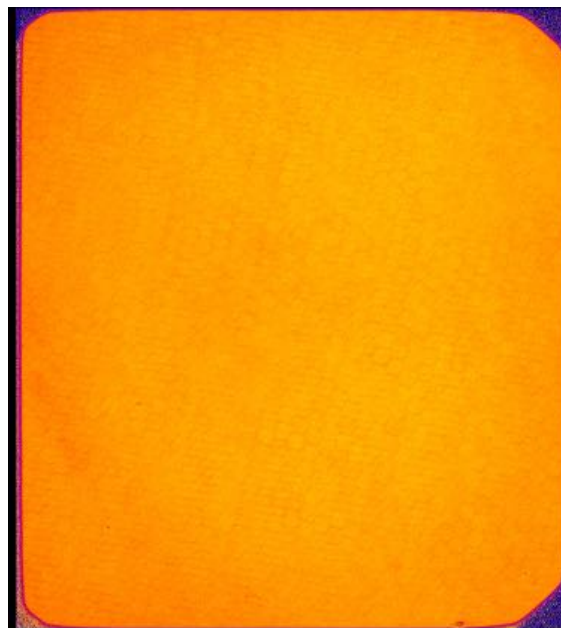


Figure 10: Full field gain map image (185 nm UV) of the GOLD FM03 detector showing the faint gain modulation due to the MCP hexagonal multi-fibers (measured at $\leq 10\%$ less).

3.4 Spatial Resolution and Image linearity

The spatial resolution for the GOLD detectors was determined with a mask placed in direct contact with the top MCP, illuminated with 185 nm light. The mask has 10 μm holes and 1 mm spacing with positional accuracy to better than 10 μm . Accumulated images (Fig. 11) were taken with flight electronics at a range of gain values to determine the resolution point spread function and the image non-linearities. Measurements of the image distortions show that there are image displacement, the most prominent being at the upper and lower right corners of the image – as expected. However, the image positions are stable and the image non-linearity characteristics are correctable to better than the ~ 50 μm level. The GOLD detector spatial resolutions (Fig. 12) were measured with laboratory electronics and flight electronics packages using the point spread distributions of the images of the mask pinholes. At the lower gains the S/N of the amplifiers dominates, but at higher gain the intrinsic timing jitter of the electronics constant fraction discriminator becomes the limiting factor. Due to power limitations for the flight implementation of the GOLD electronics parts used for the constant fraction discriminator and time to amplitude converters were not as good as the laboratory circuits. This led to poorer resolution performance, but which was adequate to meet flight requirements of <60 μm , while still meeting our overall power specifications. Typical flight spatial resolution performance was ~ 55 μm FWHM at 1×10^7 gain.

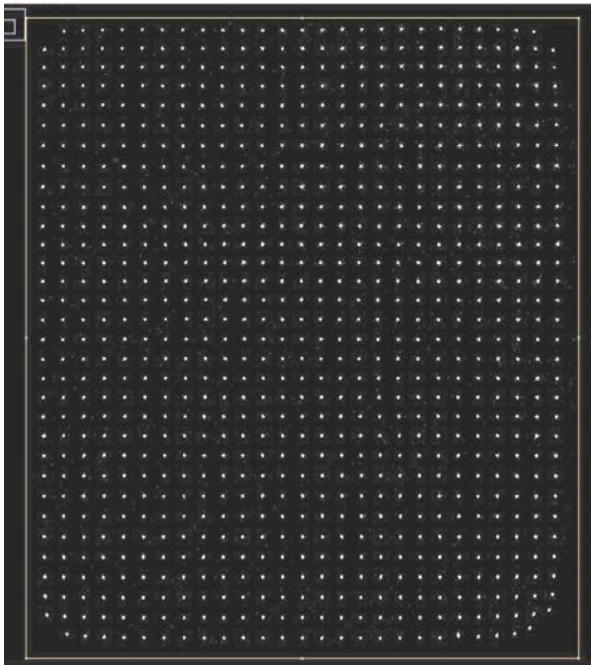


Figure 11: Image for GOLD FM01 detector with flight electronics, mask with 10 μm holes and 1mm spacing using 185 nm UV. Measurements of image distortion show stable image nonlinearity correctable to $< 50\mu\text{m}$.

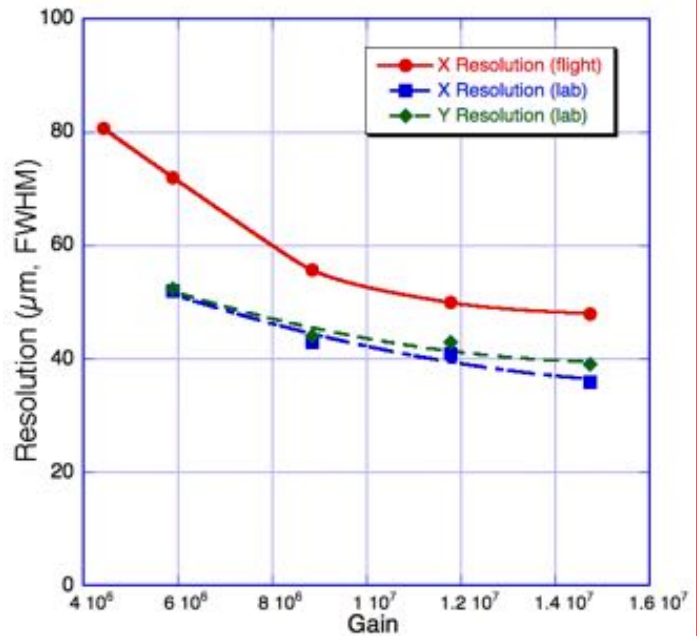


Figure 12: GOLD FM02 detector spatial resolution with laboratory and flight electronics. At the lower gains the S/N of the amplifiers dominates, but at higher gain the intrinsic timing jitter of the electronics constant fraction discriminator becomes the limiting factor.

3.5 Event Rate Handling and Gain Stability

The event rate handling capability of the GOLD detector systems is determined by two main factors. One is the ability of the electronics to process the incoming events, determining the global event rate characteristics. A second is the ability of the MCPs to accept sequential events in the same location without a decrease of the local gain which may cause events to be missed. The event handling capability of the GOLD electronics is largely determined by the time to digital converter processing time for the components chosen to meet the GOLD flight requirements. This time is also affected by the signal sampling settings and FPGA processing sequence. The typical GOLD event processing time is in the region of 700ns to 900ns which achieves (Fig. 13) a dead time of $\sim 10\%$ at event input rates of ~ 200 KHz. Events arriving immediately after the event processing period can be accepted and encoded thus establishing a non-paralyzable dead time where rates well above 200 KHz can be accommodated but with proportionately increasing dead time percentage.

The local event rate limit is determined by the recovery time of the MCP pores⁷ that are involved in the amplification of an event. The resistance of the MCPs and their configuration play a part in setting the expected recovery time. If events occur in the same location before the pores have “recharged” the gain may be reduced. As long as this reduction is modest (<20% reduction) no degrading imaging effects will be observed. Prior data⁷ for MCPs has shown that the local maximum rate of ~ 5 events pore⁻¹ sec⁻¹ for GOLD can be easily exceeded (~ 15 events pore⁻¹ sec⁻¹) provided that the resistance of the MCPs used (46 mm diameter, 3 MCP stack) is in the region of $\sim 100 - 150$ M Ω . Typical GOLD MCP stack resistances are within this range.

Another issue that pertains to the GOLD MCP stability is that of gain “burn-in”. Since these detectors are “open –face” and subjected to dry N₂ storage before launch activities they cannot be permanently “burned-in” to stabilize the MCP gain. In common with most MCPs a “burn-in” conditioning produces a drop in gain that can then be recovered by increasing the MCP potential. Results with the GOLD MCPs (Fig. 14) are in accord with previous experience³ and drop in gain by about a factor of 20 during burn-in to ~ 0.25 C cm⁻² when operated at low gain ($\sim 2 \times 10^4$). Subsequent exposure to dry N₂ does result in the gain partially recovering (Fig. 14), so a capability for burn-in of the MCPs using a UV source has been implemented for post launch operations.

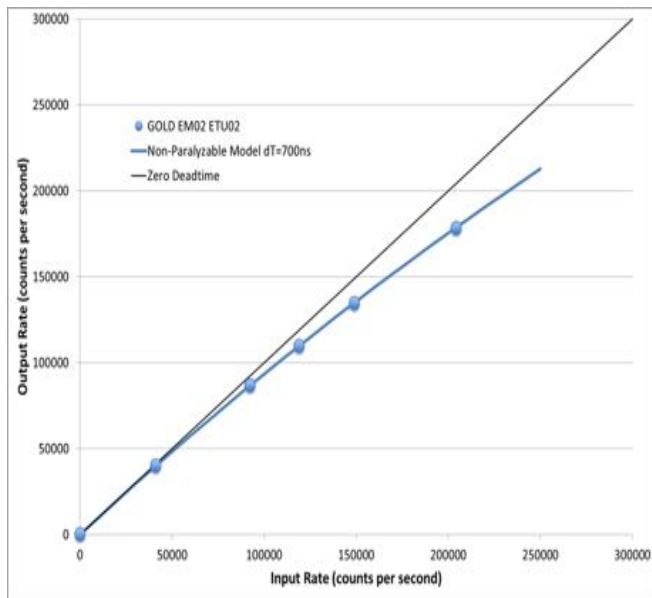


Figure 13: Electronics high rate performance is set by the non-paralyzable dead time of the electronics, which is ≥ 700 ns (mostly determined by the time to digital converter) giving $\sim 10\%$ deadtime at 200 KHz.

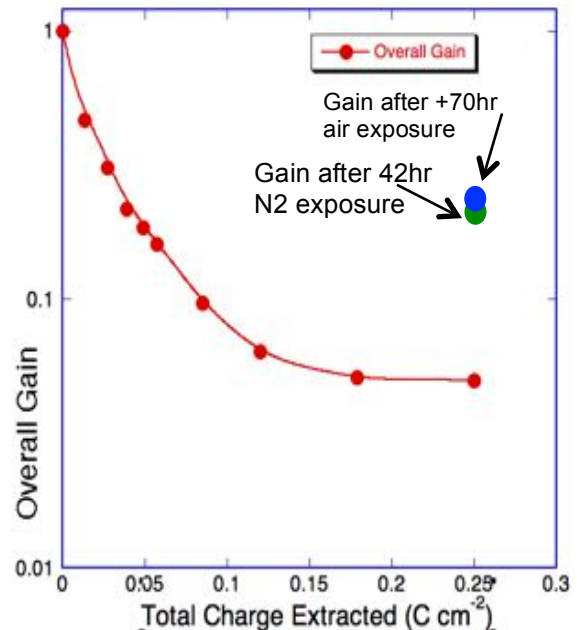


Figure 14: Gain as a function of total extracted charge during a “burn-in” of a GOLD MCP stack. Burn-in was performed with an overall gain of $\sim 2 \times 10^4$ and ~ 4 μ A output current. Subsequent exposure to dry N₂ partially restores the gain.

3.6 Quantum Detection Efficiency

The quantum efficiency of the GOLD detectors is determined by the CsI photocathode and MCP performance. Deposition of CsI opaque⁸ photocathodes onto the top of the first MCP is a standard technique for enhancement of FUV QE. Quantum detection efficiency measurements for the bare MCPs is measured first because it has been found⁶ that the secondary electron detection efficiency of the MCPs can play an important part in the determination of the QE both before and after the CsI photocathode deposition. To characterize the quantum efficiency of the detectors, they were installed into a large vacuum chamber fitted with a three-axis manipulator, a monochromator, calibrated NIST reference photodiodes and a hollow cathode gas discharge source producing EUV and FUV emission lines. The initial measurements for the bare GOLD MCPs (Fig. 15) indicated a modest, but not optimal QE compared with previous experiences⁹. We investigated the QE as a function of the gain and of the bias applied to the top MCP. For low applied voltage to the top MCP the QE increases with increasing gain (Fig. 16) and incremental bias voltage. However,

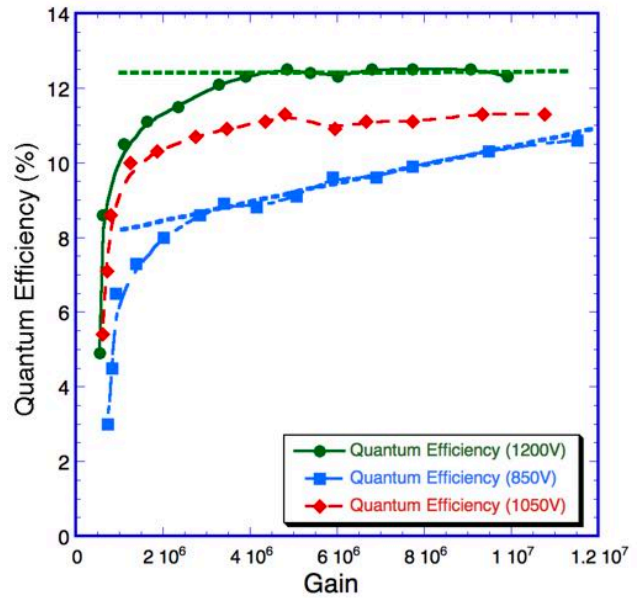
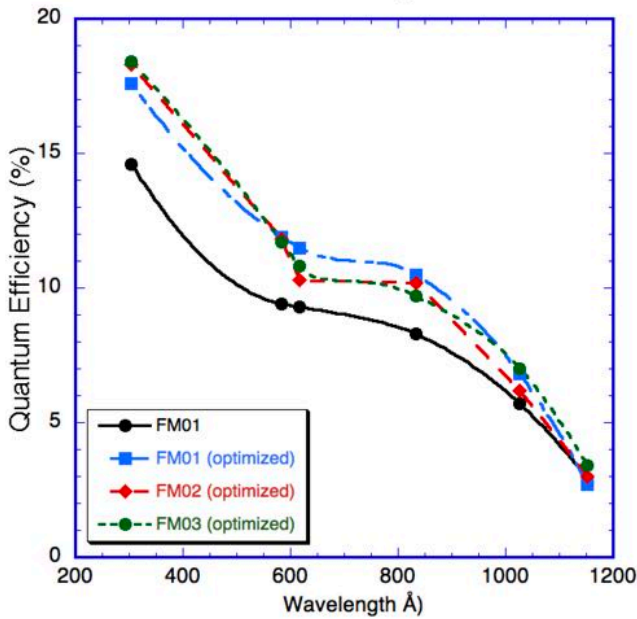


Figure 15: Bare MCP Quantum efficiencies vs. wavelength for three of the GOLD flight MCP stacks. Initial resistance matched MCPs for the FM01 detector were marginally lower than expected. Subsequent MCP stacks were adjusted to increase the bias on the front MCP thereby increasing the quantum efficiency.

Figure 16: Quantum efficiency at 584Å of a GOLD MCP stack vs. gain for three different top MCP bias configurations (@ 8×10^6 gain). At low bias the QE increases with gain but at higher bias the QE is constant once the event counting threshold is exceeded.

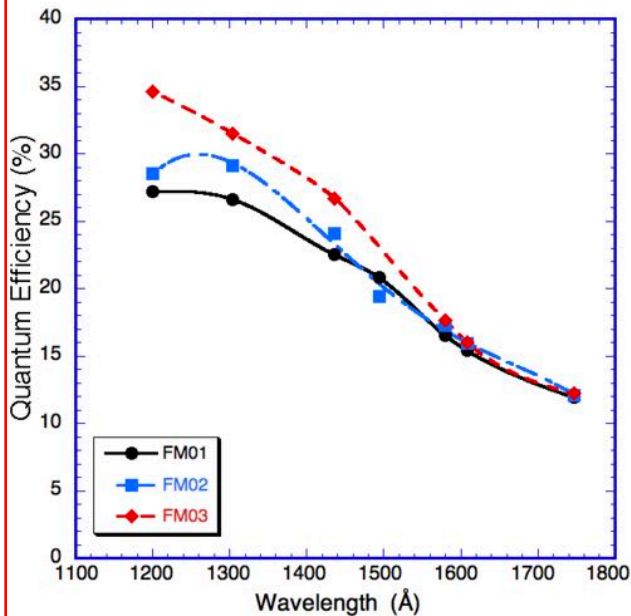


Figure 17: GOLD flight detector CsI photocathode QE as a function of wavelength at normal incidence to the MCPs. The QE is optimized by using a configuration with higher bias on the top MCP. Achieved values compare well with HST-COS³.

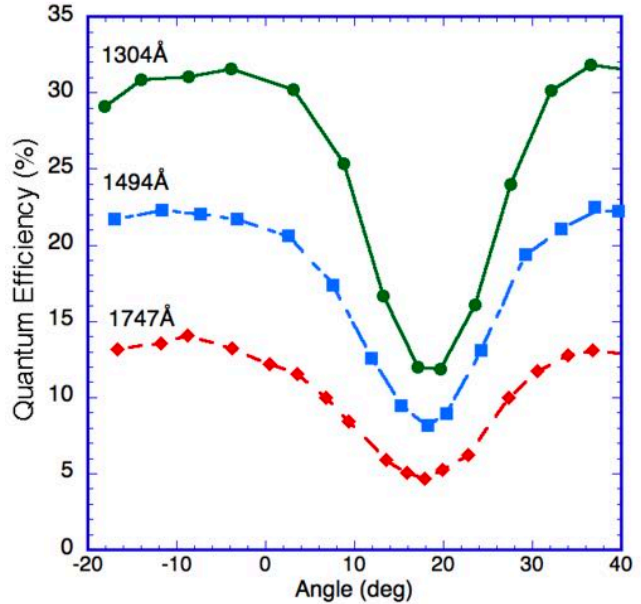


Figure 18: Quantum efficiency curves vs. incident angle, at three wavelengths, with a front field bias applied between the input MCP and the entrance grid. As expected the QE is minimized when light is directed straight down the MCP pores at 19°.

by preferentially increasing the bias of the top MCP the QE becomes independent of the gain. This indicates that at sufficient top MCP bias the secondary electron detection efficiency is maximized. So for all GOLD MCP stacks the top MCP resistance was chosen so that the top MCP bias was $\sim 15\%$ higher than the rest. The result (Fig. 15) was an optimal QE for the bare MCPs, and subsequently CsI coated MCPs were in the same range as that achieved for HST-COS (Fig. 17)³. In all cases a bias of ~ -600 V was applied to the 95% transmissive grid mounted ~ 6 mm above the MCPs, which serves to divert the photoelectrons emitted away from the MCP surface⁸ back down onto the MCPs and enhance the quantum efficiency by up to 30%. The angular variation of the QE shows (Fig. 18) was also measured and shows a minimum at the MCP pore bias angle (photons straight down the channels). The QE peaks at $\sim 19^\circ$ to the MCP face for 1304Å and at slightly larger angles at longer wavelengths. This is as expected⁸ and is controlled by the competing factors of small angle reflectance and the photoelectron escape depth at larger input angles. The QE variation across the face of the detector is relatively small ($< \pm 10\%$).

The effect of the QE enhancement grid on the detectors does increase the QE but also shadows some of the incoming flux. The 95% transparency does limit the loss and the angle distribution of the incoming optical beam ensures that the grid shadows are not sharp. However the shadows that can be observed in a test setup with an almost parallel UV beam (Fig. 19) allow the potential effects of the photoelectron “halo” due to the electrons collected from the MCP web area. The depth of modulation due to the grid shadows is maximized if the grid bias is 0 V or -20 V since no photoelectrons are collected in these cases. The modulation also is similar for 600 V and 800 V grid bias indicating minimal broadening of the spot resolution. However, at 100 V or 200 V extra bias the modulation contrast is visibly reduced and is caused by photoelectrons falling further away from the photon point of origin, as expected from earlier estimations⁹. Therefore we have established grid bias fields of about 600 V for all the flight detectors. One further test was to check the grid image as a function of event rate to establish that high global rates do not blur the spatial resolution. Fig. 20 demonstrates that here is no visible degradation of the grid image shadow modulation up to 200 KHz global rates which verifies the processing electronics stability.

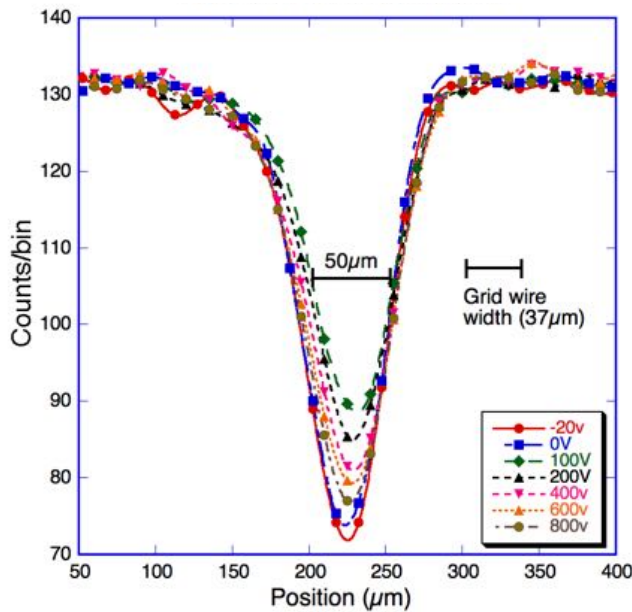


Figure 19: Histogram of the shadow of a grid wire of the QE enhancement grid. The FWHM does not widen due to the photoelectron “halo” until the MCP-Grid bias is < 200 V.

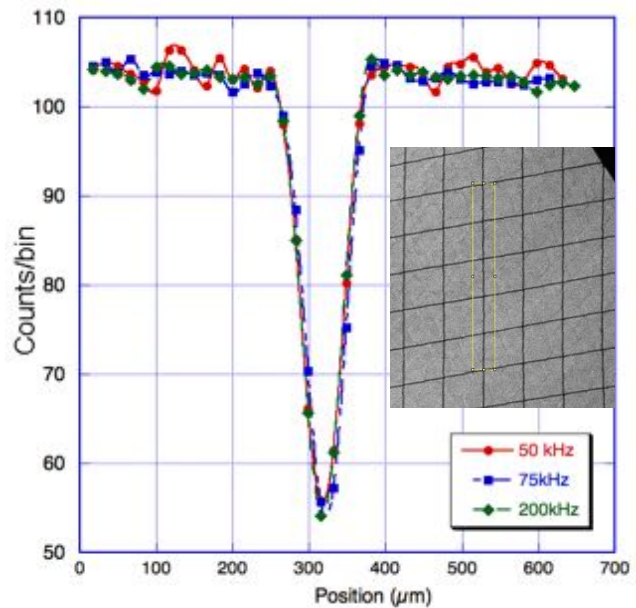


Figure 20: The same test configuration as in Figure 19, was used to evaluate resolution as a function of counting rate up to 200 KHz (no degradation was seen at the highest rates).

4. SUMMARY

Two engineering and three flight model open face MCP detectors have been successfully constructed for the GOLD instrument. These meet the performance specifications and two are in the process of being integrated into the overall instrument. Vibration tests and thermal vacuum tests have been done successfully and other environmental and performance tests at this level are in progress.

5. ACKNOWLEDGEMENTS

The authors would like to thank the LASP, UCF and SSL GOLD project teams for ongoing support in development of the GOLD detectors and electronics. This effort was supported by NASA contract NNG12PQ28C.

REFERENCES

- [1] Eastes, R. W McClintock, A. Burns. "Global-scale Observations of the Limb and Disk (GOLD) Mission - Observing Forcing of the Thermosphere-Ionosphere System from Above and Below", Joint American Astronomical Society/American Geophysical Union Triennial Earth-Sun Summit, meeting #1, id.109.01 (2015).
- [2] Siegmund, O. H., Jelinsky, P. N., Jelinsky, S. R., Stock, J. M., Hull, J. S., Doliber, D. L., Zaninovich, J., Tremsin, A. S., and Kromer, K. "High-resolution cross delay line detectors for the GALEX mission", Proc. SPIE 3765, 429, (1999).
- [3] Vallergera, J.V., McPhate, J. B., Martin, A. P., Gaines, G. A., Siegmund, O. H., Wilkinson, E., Penton, S., and Beland, S. "HST-COS far-ultraviolet detector: final ground calibration," Proc. SPIE 4498, 141-151, (2001).
- [4] Fraser G.W., J.F. Pearson, G.C. Smith, M. Lewis and M.A. Barstow, "The gain characteristics of microchannel plates for X-ray photon counting", IEEE Transactions on Nuclear Science, Vol. NS-30, No. 1, (1983).
- [5] Siegmund, O.H.W., Vallergera, J., and Wargelin, B., "Background Events in Microchannel Plates," IEEE Trans. Nucl. Sci., NS-35, 524-528 (1988).
- [6] Siegmund, O., Vallergera, J., Tremsin, A., and McPhate, J. "Microchannel plates: recent advances in performance," Proc. SPIE 6686, (2007).
- [7] Siegmund, O.H.W. Amplifying and position sensitive detectors, in "Methods of vacuum ultraviolet physics" Chapter III, 2nd edition, ed's J.A.R. Samson and D.L. Ederer, Academic Press, (1998).
- [8] Siegmund, O.H.W., Everman, E., Vallergera, J., and Lampton, M., "Extreme Ultraviolet Quantum Efficiency of Opaque Alkali Halide Photocathodes on Microchannel Plates," Proc. SPIE 868, 18-24 (1987).
- [9] Taylor, R.C., M.C. Hettrick, and R.F. Malina, Rev. Sci. Instrum. **54**, 171 (1983).